Boundary-Layer Meteorol (2009) 133:323–341
DOI 10.1007/s10546-009-9406-2

ARTICLE

Quantifying the Spatial Variability of Surface Fluxes Using Data from the 2002 International H2O Project

Joseph G. Alfieri · Dev Niyogi · Hao Zhang · Margaret A. LeMone · Fei Chen

Received: 20 October 2008 / Accepted: 23 June 2009 / Published online: 21 July 2009

Abstract Spatial variability in the exchange of energy and moisture is a key control on numerous atmospheric, hydrologic, and environmental processes. Using observations made on fair weather days during the 2002 International H2O Project, four methods for quantifying the spatial variability of surface fluxes are investigated. The first two methods utilize applied statistical techniques to describe the spatial variability of the surface fluxes, while the third method is a geostatistical technique rooted in variography. Typically, the methods yield similar results, with median values of horizontal variability consistent to within 5%. The geostatistical technique, however, provides much more information than the other statistical methods; it not only provides an estimate of the spatial variability, but also provides estimates of the total variability, the non-spatial variability due to measurement error, and the range of spatial correlation among the data points. The fourth method is based on the relationship between the components of the surface energy budget. This method describes the variability in the fluxes in terms of the slope of the best-fit line relating the time-averaged latent and sensible heat fluxes from different locations along the flight path. The meaning of the slopes can also be interpreted in terms of the spatial variability in the available energy. For four of the five days analyzed, the key control on the spatial variability in the turbulent heat fluxes was horizontal variability in the soil heat flux. In turn, the soil heat flux varied as a function of surface properties including surface temperature, soil moisture content, and leaf area index. On the remaining day, 25 May, the primary control was the variability in net radiation.

Keywords Airborne observations · IHOP_2002 · International H2O Project 2002 · Spatial variability · Surface energy fluxes

J. G. Alfieri · D. Niyogi (✉) · H. Zhang
Purdue University, 915 West State Street, West Lafayette, IN 47907, USA
e-mail: dniyogi@purdue.edu

M. A. LeMone · F. Chen
National Center for Atmospheric Research, Boulder, CO 80307, USA

1 Introduction

Land-surface characteristics exert an important control on the exchange of energy and moisture between the land surface and atmosphere, and on the partitioning of the surface energy budget. For example, surface characteristics such as the type, distribution, and density of vegetation affect albedo and the emission of longwave radiation (McPherson 2007). Dense transpiring vegetation also tends to reduce the soil (G) and sensible (H) heat fluxes by preferentially partitioning energy into the latent heat flux (λE; Segal et al. 1988).

Due to their influence on land-atmosphere exchange processes, land-surface characteristics also exert control over numerous atmospheric, hydrologic, and environmental processes. For example, variations in land cover affect the evolution of the boundary layer (Santanello et al. 2007), while the distribution of vegetation and soil moisture influences the development of local circulations (Anthes 1984; Raddatz 2007) and precipitation (Pielke 2001; Pielke et al. 2007) patterns. Variations in surface exchange processes have also been tied to the degree of precipitation recycling (Raddatz 2005) and changes in the diurnal temperature range (Durre and Wallace 2001).

In order to investigate many surface exchange processes, it is necessary to collect measurements of surface fluxes and the factors controlling them across large areas. This is often accomplished using airborne observations (e.g. Sellers et al. 1995; Oncley et al. 1997; Song and Wesley 2003; Stassberg et al. 2008). Accurately describing the spatial variability in the airborne measurements of surface fluxes is an important prerequisite for using such data to investigate subsequent environmental processes such as the evolution of the boundary layer. However, obtaining a sufficient sample to characterize the variability of airborne observations can be challenging (Mann and Lenschow 1994).

Using observations made as a part of the 2002 International H2O Project (IHOP_2002; Weckworth et al. 2004; LeMone et al. 2007b), three statistical methods for quantifying the spatial variability of airborne observations of surface fluxes were investigated. The first of these methods defines the variability in terms of the spatial standard deviation of the flux measurements; the second estimates the spatial variability as the asymptotic value of a relation between the spatial standard deviation of the airborne flux measurements to the number of flight legs, i.e. passes along the flight track (Mahrt et al. 2001); the third method uses a geostatistical technique to estimate the spatial standard deviation of the airborne surface-flux measurements. While the geostatistical method has been used in a number of other fields—for example, remote sensing (Garrigues et al. 2006)—one of our objectives is to test its applicability to airborne surface-flux measurements. Moreover, because the method is statistically robust and straightforward to implement, it may prove to be a valuable method not only to quantify the spatial variability in airborne flux measurements, but also to explore those measurements statistically.

The fourth method for describing the spatial variability of surface-flux estimates is rooted in the relationship described by the surface energy balance. This method builds on the technique developed by LeMone et al. (2003, 2007a) that uses the slope of the best-fit line relating the horizontally distributed estimates of λE to estimates of H in order to explore the interrelationships between the surface fluxes. This analysis method has been extended to include the slope of the available energy (A), i.e. the sum of the turbulent fluxes, as a function of H. The study takes advantage of this method, as well as data collected at the IHOP_2002 surface sites, to identify the potential causes of the variability observed in the airborne flux estimates.

The following section provides a brief overview of the IHOP_2002 field campaign and describes the data used herein. The third section describes the analysis methods, while Section 4 discusses the results. Finally, the conclusions are presented in Section 5.

2 Site and Data Description

2.1 2002 International H2O Project

Although a full description of the IHOP_2002 field campaign can be found elsewhere (e.g. Weckworth et al. 2004; LeMone et al. 2007b), a brief summary of IHOP_2002 is provided here. IHOP_2002 was a multi-agency field campaign conducted from 13 May to 25 June 2002 in the southern Great Plains of the U.S.A., specifically, in portions of Kansas, Oklahoma, and Texas (Fig. 1). The research domain incorporated a broad range of environmental conditions. For example, a strong east-west precipitation gradient existed across the domain, with the semi-arid western portion of the domain experiencing severe drought and the climatologically moist eastern portion of the domain, which was located in the Walnut River Watershed, experiencing a water surplus. The elevation decreased by approximately 520 m, from 870 m in the western portion of the domain to approximately 350 m in the east. The research domain also represented a broad range of land cover types, from bare ground and cropland (primarily winter wheat) to grassland and sagebrush rangeland.

2.2 Surface Data

A complete description of the surface data from the IHOP_2002 field campaign, including the instrumentation and post-processing methods, can be found in LeMone et al. (2007b) and at http://www.ral.ucar.edu/research/land/observations/ihop.php. A brief overview is given here. Surface data including meteorological, radiometric, energy flux, soil and surface properties were collected at 10 surface sites distributed across the IHOP_2002 domain (Fig. 1). The meteorological data collected at the surface sites included air temperature (T_a), mixing ratio (q), wind speed (U), and turbulent fluxes H and λE, with the fluxes obtained using the eddy-covariance method. With the exception of wind speed, which was measured at 10 m, all of these variables were measured at a height of 2 m above ground level.

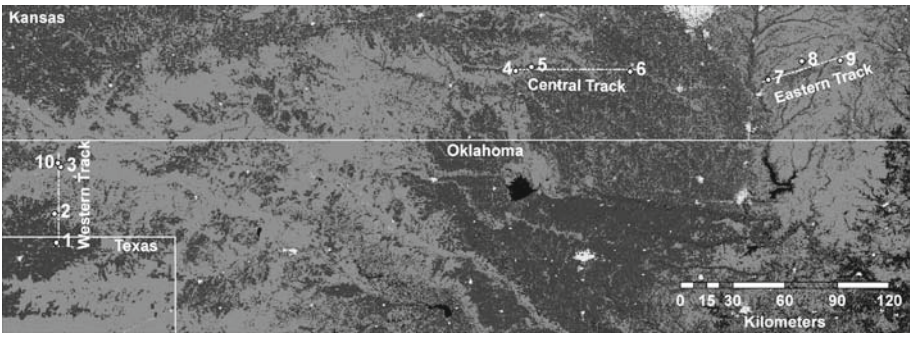

Fig. 1 The locations of each of the IHOP_2002 surface sites and their associated flight tracks are shown

Table 1 IHOP_2002 flights considered in this analysis

Date	Track	No. flight legs at 60–70 m agl	Cloud cover
25 May 2002	Western	10	Clear
29 May 2002	Western	5	Scattered
30 May 2002	Eastern	8	Clear
31 May 2002	Central	7	Nearly clear
22 June 2002	Eastern	10	Nearly clear

Site measurements also included radiometric data including incident solar radiation ($K\downarrow$), incident longwave radiation ($L\downarrow$), net radiation (R_n), and surface temperature (T_{sfc}); soil data included the soil heat flux (G), volumetric soil moisture content (θ), and soil temperature (T_{soil}), all measured at a depth of 0.05 m. The meteorological and soil data were collected as 5-min block averages that were post-processed using a standard suite of corrections including a coordinate rotation (Wilczak et al. 2001) and the density correction (Webb et al. 1980) and aggregated to 30-min block averages. Finally, surface conditions were characterized approximately every 10 days using measurements of normalized difference vegetation index (NDVI), greenness fraction (F_g), and leaf area index (LAI). The greenness fraction was determined following Gutman and Ignatov (1997) using the constants for minimum and maximum NDVI derived for the IHOP_2002 domain reported in Alfieri et al. (2007).

2.3 Airborne Observations

The aircraft data used in this study were collected during five fair-weather days during the IHOP_2002 field campaign (Table 1) using the University of Wyoming King Air aircraft. Data were collected along 5–10 straight-and-level flight legs at 60–70 m above the surface and along one of three 45–60 km flight tracks (Fig. 1). Further information can be found in LeMone et al. (2007b) and at http://flights.uwyo.edu.

The turbulent fluxes, H and λE, were estimated from the fluctuations in the vertical wind speed (w'), potential temperature (Θ') and mixing ratio (q') relative to their respective linear trends for the whole of the flight track after truncation to ensure that all of the flight legs had the same endpoints. Using the fluctuations relative to the linear trend of the entire flight track is necessary to account for large-scale eddies when calculating the fluxes from the products $w'\Theta'$ and $w'q'$. The products were averaged as a 4-km running average with a 1-km interval. The overlapping 4-km means were then averaged in time to obtain the grand-average leg. Except for truncating the flight legs to ensure averages at the same points, this procedure is identical to that described in LeMone et al. (2003, 2007a). These flux estimates were extrapolated to the surface assuming a linear flux profile, as in LeMone et al. (2008).

Additionally, radiometric fluxes, including both incident and upwelling shortwave radiation ($K\uparrow$) and incident and upwelling longwave radiation ($L\uparrow$), and surface properties such as T_{sfc}, NDVI, and albedo (α), were estimated from the airborne measurements. In addition, R_n along the flight track was estimated using the four-component radiation measurements as follows:

$$R_n = K\downarrow - K\uparrow + L\downarrow - L\uparrow . \quad (1)$$

3 Methodology

3.1 Statistical Analysis Methods

The spatial analysis combines three methods: the first method that quantifies spatial variability simply calculates the spatial standard deviation and mean using the grand-average data. The second method extends the spatial statistical technique proposed by Mahrt et al. (2001), and defines the spatial variability as the asymptotic value of the standard deviation of the observations along the flight track as the number of samples (flight legs) included is increased. The third method utilizes the geostatistical concept of variography to estimate not only the spatial variability, but also the non-spatial variability (i.e. measurement error), spatial mean, and practical range of spatial correlation among the measurement points.

3.1.1 Asymptotic Method

Extending the technique of Mahrt et al. (2001), for a flight consisting of a series of N flight legs (y_t), each corresponding to a time t and having j co-located measurements along the flight path, the temporal variability in the observations is calculated in five steps. The first step is to produce n_k mean flight legs $\left(\bar{y}_{k_m}\right)$ by averaging together all n_k possible combinations of k flight legs. The spatial standard deviation $\left(\sigma_{k_m}\right)$ of each $\bar{y}_{k_m}$ is then taken and the average spatial standard deviation ($\bar{\sigma}_k$) is computed. Finally, $\bar{\sigma}_k$ is plotted as a function of k yielding a curve that asymptotes to a constant value (σ_{asym}) indicative of the degree of spatial variability within the observed data. The data are then fitted to an exponential decay function of the form

$$\sigma_{k,l} = \sigma_{asym} + ae^{-bk} \tag{2}$$

where σ_{asym}, a and b are fitted constants. The fitted value of σ_{asym} is then taken to be the spatial variability along the flight path. Because the data rarely show a clear asymptote, the curve fitting step provides a more accurate estimate of the asymptote than determining it subjectively.

In addition to the curve-fitting step, this method differs from that described by Mahrt et al. (2001) by considering all possible combinations of flight legs when generating the asymptotic curve. The method described earlier adds flight legs via serial additions to the number of flight legs; i.e., it considers the first flight leg, then the average of the first two flight legs, then the average of the first three flight legs, and so on until all of the flight legs are averaged together. As illustrated by Fig. 2, which compares the Mahrt et al. (2001) technique to the extended version just described, including all possible combinations of flight legs in each average leads to a smoother convergence towards a stable estimate of the spatial variability.

3.1.2 Geostatistical Method

Variography is a well-established geostatistical technique that is accepted across a broad range of fields ranging from mining and agriculture to hydrology and ecology. For example, variography has been used in analyzing satellite data (e.g. Woodcock et al. 1988a,b; Garrigues et al. 2006; Tarnavsky et al. 2008), to investigate geological processes (Chappell et al. 2003; Sertel et al. 2007), and to enhance agriculture and silviculture (Ersahin 2001; Kint et al. 2003). Nonetheless, its use in the atmospheric sciences has been limited. To the authors' knowledge, this is the first time the technique has been applied to airborne observations in order to quantify spatial variability.

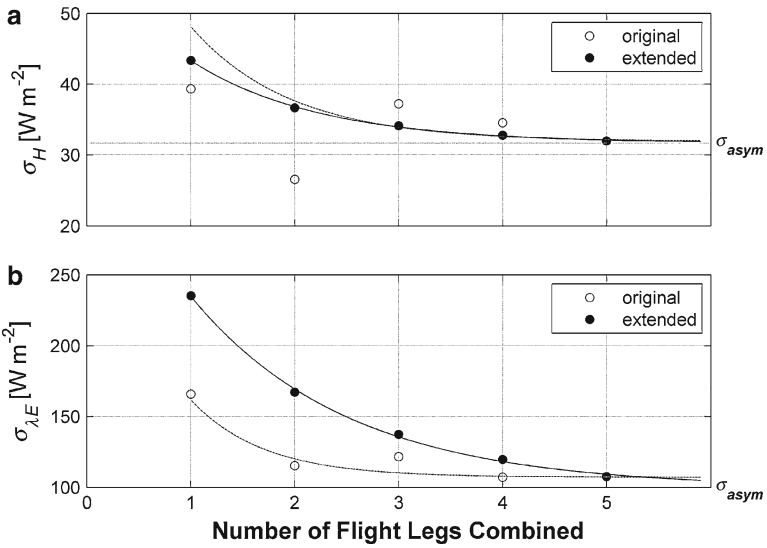

Fig. 2 The values of σ_k derived from the aircraft measurements of the (**a**) sensible and (**b**) latent heat fluxes collected during the 29 May 2002 flight are shown for the technique described by Mahrt et al. (2001) and the extended method. Both the best fit exponential decay curves associated with each method and the asymptotic values (σ_{asym}) representing the spatial variability estimated using the exponential decay function for extended method are also shown

Variography is built on the regionalized variable theory that treats the spatial data as one realization of some underlying spatial process (Cressie 1993) with a second-order stationarity. That is, the underlying process has a constant mean and covariance that depends only on the lag distance (h) between points (Schabenberger and Gotway 2005). Under these conditions, the degree of relationship or correlation between the observation locations can be determined as the semivariance (γ), which is defined as a function of h according to

$$\gamma(h) = \tau^2 + \sigma^2 [1 - C(h)] \tag{3}$$

where τ^2 is the non-spatial variance, σ^2 is the spatial variance and $C(h)$ is a valid covariance function. A valid covariance function is positive definite and fulfils the assumption of spatial continuity, i.e. proximal locations are more strongly related than more distant ones (Isaaks and Srivastava 1989).

To illustrate this method, consider the simulated data used to create Fig. 3. The simulated data were generated be selecting 50 random points from a normal distribution with a mean of 100 and variance defined using the Gaussian covariance function with maximum variance (σ^2) of 10 and a range of 2. The fitted variogram estimates the mean of the data (β) as 99.37, the non-spatial variance (τ^2) as 0, the spatial variance (σ^2) as 9.91, and range (ϕ) as 2.09.

In practice γ is estimated following a three-step process. First, the semivariance is calculated for all possible combinations of observations and presented as a scatter plot to produce a semivariogram cloud (Fig. 3a), via

$$\gamma(h) = \frac{1}{2|N(h)|} \sum_{N(H)} [z(u) - z(u+h)]^2 \tag{4}$$

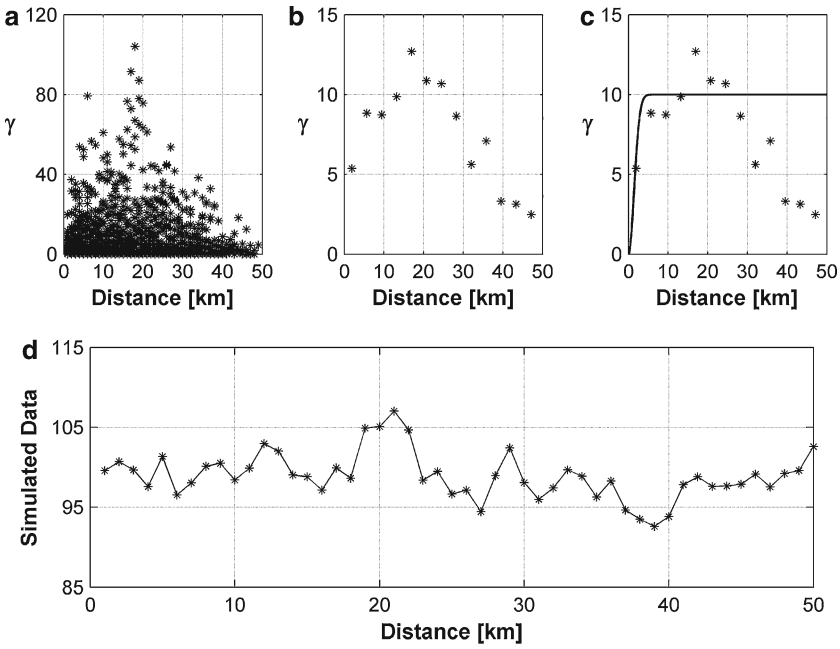

Fig. 3 The semivariogram cloud (**a**), empirical semivariogram (**b**), and fitted semivariogram (**c**) are shown for the simulated data (**d**). Note that, while only distances less than 25 km are used when fitting the semivariogram, the complete dataset is shown

where z is a variable, and $|N(h)|$ is the number of paired points for lag distance h along the flight track. These values are then bin-averaged as a function of the separation distance between the locations of the pair of observations. This produces an empirical semivariogram (Fig. 3b). Finally, the semivariogram function is determined by fitting the empirical semivariogram to an appropriate model using the restricted maximum likelihood method (Fig. 3c). For this step, only distances less than or equal to one-half of the maximum lag distance are used because the number of points contained within each bin decreases with increasing lag distance. As a result, the number of points may not be sufficient to provide statistically meaningful results when the lag distance is large. Restricted maximum likelihood is well known to outperform the ordinary least-squares method in that it has superior predictive performance as measured by the mean squared error (Zimmerman and Zimmerman 1991; Zhang 2004; Zhang and Zimmerman 2007). Maximum likelihood estimators are generally more efficient (i.e., having smaller variances) than the least-squares-based methods (Zimmerman and Zimmerman 1991), particularly when the sample size is small (Diggle et al. 2003).

The resulting curve (shown as an idealized curve in Fig. 4) allows one to estimate the spatial variance (σ_V^2), the non-spatial variance (τ^2), the total variance ($\sigma_V^2 + \tau^2$; referred to as σ_{tot}^2 hereafter), and the range of spatial correlation (ϕ) of the data. The non-spatial variance represents all the non-spatial variability, including the uncertainty in local values due to a small sample size or measurement error. For example, in the field of geology, error is introduced in the measurements of features in sediments by the size of the component particles; hence the non-spatial variance is often called the "nugget effect."

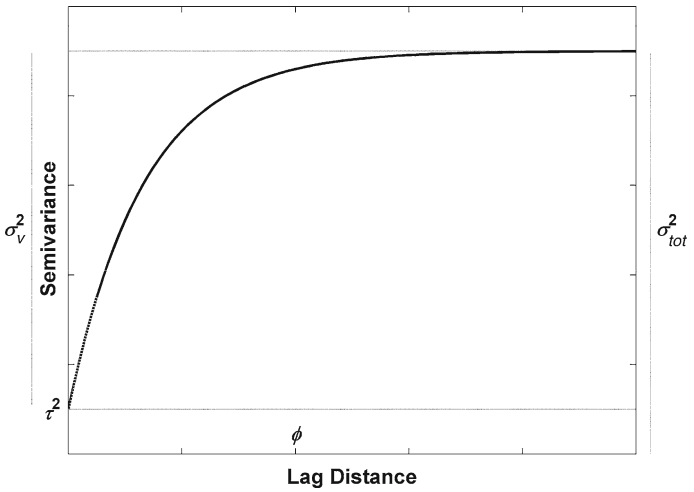

Fig. 4 An idealized semivariogram curve showing the total variance $\left(\sigma_{tot}^2 = \tau^2 + \sigma_V^2\right)$, spatial variance $\left(\sigma_V^2\right)$, nonspatial variance $\left(\tau^2\right)$, and practical range of spatial correlation (ϕ)

Because preliminary analysis showed it to produce the best fit of the experimental semivariograms, the Matern (1986) family of covariance functions was used as the model to fit the experimental semivariogram in this study. These functions are defined as

$$C(h) = \sigma^2 \frac{2}{\Gamma(\nu)} \left(\frac{\phi h}{2}\right)^{\nu} K_{\nu}(\phi h) \tag{5}$$

with K_{ν}, the Bessel function of the second kind, defined as

$$K_{\nu}(\phi h) = \frac{\Gamma(\nu)}{2} \left(\frac{\phi h}{2}\right)^{-\nu} \tag{6}$$

where σ^2 is the total variance, ν defines the order of the Bessel function, and ϕ defines the range of spatial correlation of the data (Schabenberger and Gotway 2005). Two special cases of this class of covariance functions are the exponential covariance function ($\nu = 0.5$) and the Gaussian covariance function ($\nu = \infty$).

The geostatistical method is also useful because it can be used to easily identify points that do not fulfil the underlying assumption of stationarity, i.e. the variance does not increase with distance between the points or the mean at a given point differs markedly from the mean of the other measurement points. The variogram cloud of such datasets often exhibits a multimodal distribution that can be used to identify the nonstationary points for further analyses. Due to its periodic behaviour, which is often the reason that the assumption of stationarity is violated, the variogram cloud of a sine wave has a multimodal distribution. Nonetheless, the geostatistical method reasonably estimates the variance. For example, the sinusoidal function

$$y = 100 + \sqrt{20} \sin\left(\frac{2\pi x}{25}\right), \tag{7}$$

Table 2 The relationship between λE, H and A for slopes (m) in different ranges. For simplicity, the relationships given assume that ΔH is not negative

Slope	λE	H	A
for $m < -1$	$\Delta\lambda E < 0$	$\lvert\Delta\lambda E\rvert > \Delta H$	$\Delta A < 0$
for $m = -1$	$\Delta\lambda E < 0$	$\lvert\Delta\lambda E\rvert = \Delta H$	$\Delta A = 0$
for $-1 < m < 0$	$\Delta\lambda E < 0$	$\lvert\Delta\lambda E\rvert < \Delta H$	$\Delta A > 0$
for $m = 0$	$\Delta\lambda E = 0$	$\Delta\lambda E < \Delta H$	$\Delta A = \Delta H > 0$
for $0 < m < 1$	$\Delta\lambda E > 0$	$\Delta\lambda E < \Delta H$	$\Delta A > 0$
for $m = 1$	$\Delta\lambda E > 0$	$\Delta\lambda E = \Delta H$	$\Delta A = 2\Delta H > 0$
for $m > 1$	$\Delta\lambda E > 0$	$\Delta\lambda E > \Delta H$	$\Delta A > 0$

which has a mean of 100 and a spatial variability of 3.16, has a mean of 99.07 and a spatial variability of 2.91 when described by the fitted variogram determined using a 50-point sample.

3.2 Slope Analysis

The slope-analysis method developed by e.g. LeMone et al. (2003, 2007a) uses the slope ($\Delta\lambda E/\Delta H$) of the best-fit line of a plot of the time-averaged λE as a function of the time-averaged H at different points along the flight track to describe variability in the surface energy fluxes. The slope technique derives from the surface energy budget,

$$R_n = H + \lambda E - G \tag{8}$$

From eq. 8, the slope (m) of a plot of λE as a function of H for points along the flight track is an indicator of the horizontal variability in the partition of the turbulent fluxes λE and H, and in A averaged over the time the data were collected. For a constant A, such a plot must have a slope of -1; all other slopes indicate horizontal variability in A. It can be seen from the surface energy balance equation that in order for the slope to have a given value, the changes in H, λE, and A must fulfil specific conditions (Table 2).

3.3 Estimation of the Soil Heat Flux and Available Energy

The initial estimates of G were calculated as the residual of the surface energy budget. Because of this, any error in the measurements of the other components of the surface energy budget are propagated into the estimates of G. In an effort to understand the degree of error introduced into the estimate of G, a test for the propagation of errors was conducted. Fortunately, the non-spatial variance (τ^2) from the geostatistical technique represents the variance of the measurements due to measurement error. As such, τ can be thought of as the standard deviation of the measurements and the maximum error can be estimated as 1.96τ. The maximum error in the estimates of $G(\Delta G)$ can then be calculated as

$$\Delta G = 3.92\sqrt{\tau_{R_n}^2 + \tau_H^2 + \tau_{\lambda E}^2} \tag{9}$$

where τ_{Rn}, τ_H, and $\tau_{\lambda E}$ are the standard deviations of the non-spatial component associated with R_n, H, and λE, respectively. (The additional factor of 2 included in Eq. 9 is necessary in this case because the 4-km data result in oversampling; this is discussed further below.) Excluding the data from 29 May, the maximum error ranged from approximately 50 W m^{-2} on 25 May to a maximum of 88 W m^{-2} on 31 May. Due to the greater uncertainty in λE on 29 May, the maximum error was nearly 190 W m^{-2}.

Table 3 Summary of the variance (**bold**) and covariance of the components of both the surface energy and radiation budgets (units of $W^2\,m^{-4}$)

Surface Energy Budget						Radiation Budget					
	R_n	H	λE	$\hat{G}$	$\hat{A}$		R_n	$K\downarrow$	$K\uparrow$	$L\downarrow$	$L\uparrow$
25 May											
R_n	**182**	−15.8	128	236	−54.5	R_n	**182**	60.2	−102	5.93	−34.9
H		**984**	−443	−557	541	$K\downarrow$		**71.4**	−5.06	3.27	10.6
λE			**1870**	1005	−877	$K\uparrow$			**127**	0.11	−11.4
$\hat{G}$				**829**	−592	$L\downarrow$				**1.04**	−3.57
$\hat{A}$					**538**	$L\uparrow$					**59.4**
29 May											
R_n	**627**	−567	1277	153	475	R_n	**627**	387	3.49	−69.2	−277
H		**1021**	−1835	247	−813	$K\downarrow$		**402**	133	−44.0	−162
λE			**11577**	−924	2201	$K\uparrow$			**135**	−8.23	−23.4
$\hat{G}$				**392**	−240	$L\downarrow$				**11.3**	41.9
$\hat{A}$					**714**	$L\uparrow$					**171**
30 May											
R_n	**67.6**	31.5	−48.6	103	−35.1	R_n	**67.6**	57.9	−14.7	3.55	9.53
H		**127.3**	−283	188	−156	$K\downarrow$		**70.0**	−0.39	7.93	19.0
λE			**3412**	−860	811	$K\uparrow$			**19.1**	2.12	−0.74
$\hat{G}$				**407**	−304	$L\downarrow$				**6.01**	7.94
$\hat{A}$					**270**	$L\uparrow$					**17.0**
31 May											
R_n	**50.8**	5.82	−8.61	49.1	1.69	R_n	**50.8**	−0.16	−36.3	3.64	−5.97
H		**552**	−410	−135	141	$K\downarrow$		**11.3**	7.98	-6.20	−4.78
λE			**2029**	179	−188	$K\uparrow$			**43.1**	−5.96	−5.10
$\hat{G}$				**87.4**	−38.2	$L\downarrow$				**6.68**	3.29
$\hat{A}$					**40.0**	$L\uparrow$					**8.73**
22 June											
R_n	**99.7**	−17.1	40.7	92.7	7.03	R_n	**99.7**	90.1	18.3	−2.87	−21.5
H		**412**	−554	126	−143	$K\downarrow$		**123**	26.9	3.30	−1.66
λE			**2379**	−253	293	$K\uparrow$			**23.9**	−2.90	−17.0
$\hat{G}$				**142**	−48.8	$L\downarrow$				**6.82**	11.4
$\hat{A}$					**55.9**	$L\uparrow$					**35.4**

Given the degree of uncertainty propagated into the estimates of G, both H and λE were recalculated by adjusting H and λE to the best-fit line, with the ratio of adjustment to both fluxes ($\delta_{\lambda E} : \delta_H$) constrained by the ratio of uncertainty in the measurements ($\tau_{\lambda E} : \tau_H$). Building on evidence in LeMone et al. (2008) that the departure of the individual points from the best-fit line relating H and λE is due to random variations, the re-calculation of H and λE minimizes the total error. For example, on 22 June, the total variability, as measured via the standard deviation, in the adjusted estimate of $H(\hat{H})$ increased slightly from $20.3\,W\,m^{-2}$ to $21.5\,W\,m^{-2}$ while the total variability in $\lambda E\left(\lambda\hat{E}\right)$ decreased from $48.8\,W\,m^{-2}$ to $29.0\,W\,m^{-2}$. The adjusted estimates are then used to calculate an estimate of $G(\hat{G})$ as a residual as follows

$$\hat{G} = R_n - \hat{H} - \lambda\hat{E}. \tag{10}$$

The available energy ($\hat{A}$) was estimated as the sum of $\hat{H}$ and $\lambda\hat{E}$; the variances and covariances associated with these estimates, as well as the other components of the surface energy and radiation budgets, are given in Table 3.

3.4 Analysis of Surface Data

The soil heat flux term, G, can expressed as

$$G = K_{soil}\frac{\partial T}{\partial z}e^{-2LAI} \cong K_{soil}\frac{T_{sfc} - T_{soil_z}}{z}e^{-2LAI} \tag{11}$$

where K_{soil} is the thermal conductivity of the soil, T_{soil_z} is the temperature of the soil at some depth, z, and LAI is the leaf area index. The term e^{-2LAI} accounts for the presence of the vegetation (Peters-Lidard et al. 1998). Both K_{soil} and the temperature gradient ($\Delta T/\Delta z$) are influenced by θ with K_{soil} increasing with increasing θ and $\Delta T/\Delta z$ decreasing with increasing θ. As a result, the effects of θ partially compensate for one another, thereby reducing the overall impact of θ on G (Small and Kurc 2003). The presence of vegetation also influences G, through surface shading and insulation, which reduces T_{sfc} and thus $\Delta T/\Delta z$. It has been suggested that T_{sfc} is linearly related to the normalized difference vegetation index (Goetz 1997); however, the relationship is complicated by numerous interconnected environmental factors such as soil thermal properties, near-surface atmospheric turbulence, and surface evaporation (Sandholt et al. 2002).

In an effort to better understand the factors controlling G, a multiple linear regression analysis was conducted using surface data collected during fair weather days. Specifically, G was regressed against T_{sfc}, LAI, θ, and R_n. By standardizing these variables, i.e. rescaling them to range between zero and one, prior to conducting the regression, it is possible to eliminate the effects of scale and use the regression coefficients to estimate the relative influence of each of the predictor variables on G (Alfieri et al. 2007). The relative influence is expressed as a percentage and is defined as

$$I_i = 100\frac{|\beta_i|}{\sum|\beta_j|} \tag{12}$$

where I_i is the relative influence of the ith variable, β_i is the coefficient associated with the ith variable, and $\sum|\beta_j|$ is the sum of the absolute values of all of the coefficients. The variable T_{soil} was not considered in the regression analysis because preliminary analysis showed that it exhibited substantial multi-collinearity with both T_{sfc} and θ. The results of this analysis are summarized in Table 4.

Table 4 Summary of the relative influence analysis conducted on the measurements of G at each surface site over the duration of the IHOP_2002 field campaign

Site	Percent variance explained	Percent relative influence			
		R_n	T_{sfc}	*LAI*	θ
1	39.1	16.5	66.6	–	16.9
2	57.3	6.7	37.3	53.5	2.5
3	72.2	6.5	6.2	45.3	42.0
4	43.8	37.1	20.3	19.9	22.7
5	51.4	6.1	45.2	25.3	23.4
6	63.3	5.9	37.5	39.7	16.9
7	71.9	3.7	28.9	59.4	8.0
8	63.9	1.3	6.1	68.5	24.1
9	70.8	5.1	13.0	43.3	38.6

Table 5 Summary of the results of variability estimates from the three analysis methods. The quantities associated with the geostatistical are shown in Fig. 4 (units in $\mathrm{W\,m^{-2}}$ except ϕ in km)

Date	Flux	σ_{GA} $\mathrm{W\,m^{-2}}$	σ_{asym} $\mathrm{W\,m^{-2}}$	τ $\mathrm{W\,m^{-2}}$	σ_V $\mathrm{W\,m^{-2}}$	σ_{tot} $\mathrm{W\,m^{-2}}$	ϕ km
25 May	H	31.4	32.3	8.9	32.7	33.9	2.87
	λE	43.2	44.5	8.9	51.2	52.0	3.50
29 May	H	32.0	31.7	6.7	30.2	30.9	4.22
	λE	108	99.7	47.8	102	112	3.14
30 May	H	11.3	11.4	3.6	12.9	13.4	4.00
	λE	58.4	58.0	18.5	64.1	66.7	3.89
31 May	H	23.5	23.6	4.8	25.6	26.0	3.36
	λE	45.0	44.6	22.0	41.5	47.0	2.83
22 June	H	20.3	20.5	3.3	20.4	20.7	4.04
	λE	48.8	50.4	14.1	49.7	51.7	3.11

4 Results

4.1 Comparison of Statistical Methods

A comparison of the results from the statistical methods shows that all three yield similar results. The estimates of spatial variability from the three methods were typically within 5% of the mean value and differed by no more than 11% (Table 5). For example, the estimates for the spatial variability in H on 25 May were $31.4\,\mathrm{W\,m^{-2}}$, $32.3\,\mathrm{W\,m^{-2}}$, and $32.7\,\mathrm{W\,m^{-2}}$for σ_{GA}, σ_{asym}, and σ_V, respectively. The mean value for the estimates on this day was $32.1\,\mathrm{W\,m^{-2}}$. The lowest value, which was associated with σ_{GA}, was 2.3% less than the mean while the highest estimate, which is associated with the geospatial method, was 1.8% greater than the mean.

The uncertainty of the measurements as determined by using both the standard error (SE) calculated using the method outlined in LeMone et al. (2003) and the method described by Mann and Lenschow (1994) was compared to the non-spatial variability (τ) estimates from the geospatial method. Allowing for some scatter, SE and the Mann and Lenschow (1994) methods yielded similar results (Table 6), though both methods yield estimates that are greater than τ.

Much of the discrepancy is due to the previously-mentioned factor-of-two underestimate of τ. This factor-of-two difference reflects the fact that the sample size is artificially inflated by the overlapping 4-km averages with an interval length of 1 km. To illustrate this, a geostatistical analysis was conducted using four sets of 4-km block-averaged data generated from the 1-km data for 25 May, and each set of block averages was offset from the previous set by 1 km. The average value of τ associated with H for the four sets of block-averaged data ($17.2\,\mathrm{W\,m^{-2}}$) was approximately twice that obtained from the analysis of the 4-km running average ($8.9\,\mathrm{W\,m^{-2}}$). Similarly, the average value of τ associated with λE for the four sets of block-averaged data ($23.7\,\mathrm{W\,m^{-2}}$) was significantly greater than the value from the 4-km running average data ($8.9\,\mathrm{W\,m^{-2}}$). Additionally, this discrepancy may be due, in part, to the fact that SE incorporates both the non-spatial variability and the temporal variability among the flight legs that contribute to the grand-average leg.

On two days it was found that the semivariogram cloud had a multimodal distribution (e.g. Fig. 5a). Using the geostatistical method, the points associated with secondary modes can be

Table 6 Comparisons of the non-spatial variability, τ, and the uncertainty for overlapping 4-km averaged fluxes as estimated by the standard error and the Mann and Lenschow (1994) method. Note that τ should be greater by a factor of 2 because the sample size is artificially inflated by a factor of four by using the 4-km running mean average data (units in $\mathrm{W\,m^{-2}}$)

Date	No. Legs	Flux	τ $\mathrm{W\,m^{-2}}$	SE $\mathrm{W\,m^{-2}}$	M & L $\mathrm{W\,m^{-2}}$
25 May	10	H	8.9	23	27
		λE	8.9	30	38
29 May	5	H	6.7	23	16
		λE	48	97	123
30 May	8	H	3.6	9.1	6.3
		λE	19	72	48
31 May	7	H	4.8	9.8	10
		λE	22	63	52
22 June	10	H	3.3	11	8.0
		λE	14	65	47

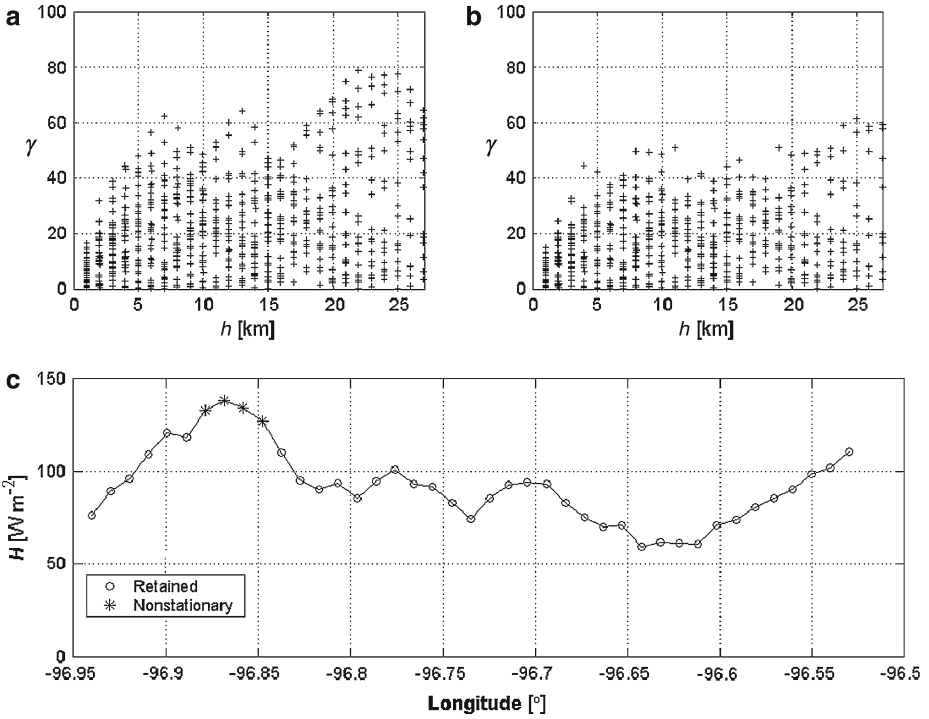

Fig. 5 The semivariogram for the sensible heat flux measurements on 22 June before (**a**) and after (**b**) points leading to nonstationarity are removed. Those points are identified in the plot of the measured flux (**c**)

identified and isolated for further analysis to ascertain whether the multimodal distribution is due to periodicity in the data or some other nonstationary effect. For example, in the case of the 22 June measurements of H, a subset of four measurements is the cause of the multimodal distribution (Fig. 5c). This subset of points with locations centred on longitude $-98.87°$ contained measurements over wheat stubble. Unlike much of the flight track, this area had been planted with winter wheat that had been harvested prior to the 22 June flight.

Table 7 Summary of the geostatistical analyses of the spatial variability using the full and parsed datasets (units in $\mathrm{W\,m^{-2}}$ except ϕ in km)

Data	Flux	Omitted points	Full dataset				Parsed dataset			
			τ $\mathrm{W\,m^{-2}}$	σ_V $\mathrm{W\,m^{-2}}$	σ $\mathrm{W\,m^{-2}}$	ϕ km	τ $\mathrm{W\,m^{-2}}$	σ_V $\mathrm{W\,m^{-2}}$	σ $\mathrm{W\,m^{-2}}$	ϕ km
30 May	λE	39–40	18.5	64.1	66.7	3.89	19.5	56.3	59.6	3.73
22 June	H	7–10	3.30	20.4	20.7	4.04	3.32	18.0	18.3	3.97
	λE	8–11	14.1	49.7	51.7	3.11	13.9	42.1	44.3	2.97

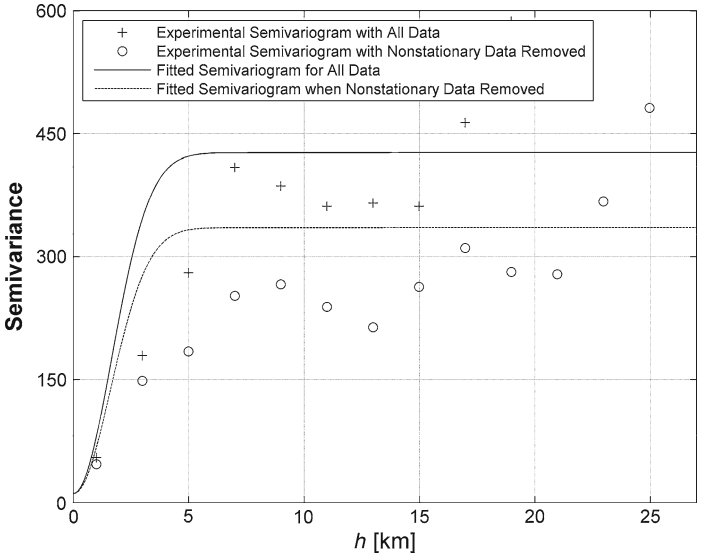

Fig. 6 The empirical and fitted semivariograms associated with the sensible heat flux measurements on 22 June are shown

The absence of vegetation in this area resulted in a greater mean H (lower mean λE) than the surrounding area.

By eliminating such points, a monomodal semivariogram cloud is produced (Fig. 5b), albeit with somewhat different characteristics than when the full dataset is used (Table 7). A comparison of the empirical and fitted semivariograms (Fig. 6) shows many of the traits that are expected; while the spatial variability is decreased, the non-spatial variability and range of spatial correlation are little changed. For example, removing the nonstationary points from the 22 June H data reduces σ_V from 20.1 $\mathrm{W\,m^{-2}}$ to 17.7 $\mathrm{W\,m^{-2}}$. The non-spatial variability (τ) decreases only by 0.02 $\mathrm{W\,m^{-2}}$ and the range of spatial correlation decreases by only 0.08 km.

4.2 Analysis of Airborne Data

The slopes of the plots of λE against H range between (Table 8) -0.45 and -2.22. In agreement with expectations that $\Delta A/\Delta H = \Delta\lambda E/\Delta H + 1$, this range of slopes corresponds to a range of slopes of the plots of $\hat{A}$ against H between 0.55 and -1.22; the y-intercepts of these plots are also equal. Furthermore, the range in $\Delta\hat{A}$ agrees with expectations in that it

Table 8 Summary of the slope analysis is given for plots of λE and $\hat{A}$ as a function H

Flight date	$\Delta\lambda E/\Delta H$			$\Delta\hat{A}/\Delta H$			Δ		
	m	b W m^{-2}	r	m	b W m^{-2}	r	H W m^{-2}	λE W m^{-2}	$\hat{A}$ W m^{-2}
25 May	−0.450	222	−0.327	0.550	222	0.389	140	−62.9	76.8
29 May	−1.80	583	−0.534	−0.797	583	−0.270	120	−215	−96.0
30 May	−2.22	648	−0.430	−1.22	648	−0.254	43.8	−97.6	−53.8
31 May	−0.745	451	−0.388	0.255	451	0.143	102	−75.9	26.0
22 June	−1.35	552	−0.561	−0.347	552	−0.172	78.9	−106	−27.1

The changes in λE, $\hat{A}$, and H are determined from the best-fit line

ranges from 76.8 W m^{-2} to −96.0 W m^{-2}. To understand such relationships, it is necessary to investigate data for each day individually.

4.2.1 Flight on 25 May

The slope for this day was −0.450 with $\hat{A}$ increasing by 76.8 W m^{-2} with increasing H along the best-fit line. The variabilities ($\sigma_{G\hat{A}}$) for this flight were 13.5 W m^{-2}, 28.8 W m^{-2}, and 23.2 m^{-2}, respectively, for R_n, $\hat{G}$, and $\hat{A}$ (Table 3 shows the variances). This, along with the larger covariance between $\hat{G}$ and $\hat{A}$ (−592 W m^{-2}) compared to that between R_n and $\hat{A}$, (−54.5) suggests that variations in $\hat{A}$ were due primarily to changes in $\hat{G}$ with R_n playing a secondary role. The high coefficient of determination (r^2) between $\hat{G}$ and $\hat{A}$($r^2 = 0.788$) further reaffirms this assessment. From Table 3, it can also be seen that the small amount of remaining variability associated with R_n is most closely tied to variations in $K\uparrow$ and thus α.

4.2.2 Flight on 29 May

For the best-fit line relating H and λE, the slope for the flight along the Western Track on this day was −1.80 with decreases in λE and $\hat{A}$ of 215 W m^{-2} and 96 W m^{-2}, respectively, as H increases along the best-fit line. In this case, however, the variances and covariances in Table 3 show that R_n is the key control on $\hat{A}$, as can also be seen by comparing the coefficients of determination; r^2 between R_n and $\hat{A}$ is 0.503 and r^2 between $\hat{G}$ and $\hat{A}$ is 0.205. Much of the variability in R_n resulted from cloud cover along the northern part of the flight track. After eliminating these points, the slope changes to −1.30 and the range in H, λE, and $\hat{A}$ become 120 W m^{-2}, 156 W m^{-2}, and 36 W m^{-2} along the best-fit line. When the points along the northern part of the flight track were eliminated, the variability in $\hat{A}$ is much more strongly linked to variations in $\hat{G}$.

4.2.3 Flight on 30 May

The flight along the Eastern Track on this day had the steepest slope, −2.22, corresponding to a change in H, λE, and $\hat{A}$ of 43.8 W m^{-2}, −97.6 W m^{-2}, and −53.8 W m^{-2}, respectively, along the best-fit line. Perhaps not surprisingly, given the lack of variation in R_n seen along this flight track (the variability in R_n, as measured by the standard deviation, for this flight was 8.1 W m^{-2}), the variability in $\hat{A}$ is most strongly linked to $\hat{G}$ (Table 3). The coefficient

of determination between $\hat{G}$ and $\hat{A}$ is 0.845, and in contrast, r^2 between R_n and $\hat{A}$ is 0.068. Indeed, over this fully vegetated region, the variation in R_n is only one-half to one-third that seen over the Western Track and is due mainly to variations in $K\downarrow$ as opposed to variations in $K\uparrow$ (Table 3).

4.2.4 Flight on 31 May

The slope of the best-fit line relating H with λE for the 31 May flight along the Central Track was -0.745, corresponding to a decrease in λE of $75.9\,\mathrm{W\,m^{-2}}$ with increasing H along the best-fit line. Also, as expected, $\hat{A}$ increased by $26.0\,\mathrm{W\,m^{-2}}$ with increasing H. Based on the statistical analysis in Table 3, the variability in $\hat{A}$ is again tied to $\hat{G}$ with R_n having only a minimal effect. The strength of the linkage is, however, weaker than on 25 May and 30 May. For 30 May, r^2 between $\hat{G}$ and $\hat{A}$ is 0.420 while it is 0.001 between R_n and $\hat{A}$.

4.2.5 Flight on 22 June

The 22 June flight along the Eastern Track had a slope of -1.35, corresponding to decreases in λE of $206\,\mathrm{W\,m^{-2}}$ and $\hat{A}$ of $27.1\,\mathrm{W\,m^{-2}}$ with an increase in H of $78.9\,\mathrm{W\,m^{-2}}$ along the best-fit line. Based on a comparison of the variances and covariances in Table 3, the cause of the variation in $\hat{A}$ is unclear. The variability of $\hat{G}$, $\hat{A}$, and R_n was $11.9\,\mathrm{W\,m^{-2}}$, $7.47\,\mathrm{W\,m^{-2}}$, and $9.98\,\mathrm{W\,m^{-2}}$, respectively. A comparison of r^2, however, suggests a stronger linkage between $\hat{A}$ and $\hat{G}$ (0.440) than $\hat{A}$ and R_n (0.008).

4.3 Analysis of the Surface Data

Given the importance of G in regulating A and thus the spatial variability of the turbulent fluxes, a further analysis of the factors controlling G along each of the flight tracks was conducted using the surface data collected during IHOP_2002 on all clear sky days. The analysis used standardized variables to estimate the relative influence of T_{sfc}, LAI, θ, and R_n on the variability in G.

As can be seen in Table 4, the predictor variables used in this analysis accounted for between 50 to 75% of the variability in G at seven of the nine sites and accounted for 58% of the temporal variability on average for all of the sites. Overall, this analysis appears most effective for the more heavily vegetated sites along the Central Track and, especially, the Eastern Track where R_n is less influential.

Overall, the analysis suggests that T_{sfc}, LAI, and θ are the key controlling factors on the variability in G, with relative importance a function of the site. Together, these three factors are linked through the shading and insulating effects of vegetation, consistent with Eq. 11. Given the consistently dry conditions along the Western Track and the water surplus along the Eastern Track, it is reasonable to suspect that vegetation density is an important control on G. Assuming the factors that influence G over time are the same as the factors controlling the spatial variability of G, this result can be linked back to the airborne observations by recognizing the high vegetation density measured by NDVI—a common proxy for vegetation density—along the Eastern Track; the mean NDVI along that track was 0.65. Additionally, the variance in NDVI was 0.02 along the Western Track, 0.05 along the Central Track, and 0.05 along the Eastern Track.

5 Conclusions

Similar estimates of spatial variability in the measured fluxes emerge from the three statistical methods examined here. There are, however, important caveats. The simple standard deviation provides information only about the overall variability of the airborne observations; as such, it provides a reasonable estimate of the spatial variability only if one assumes that the non-spatial variability is negligible. Similarly, the asymptotic method based on Mahrt et al. (2001) provides an estimate of the spatial variability only, and is limited in that the method rarely reaches an asymptotic value with the 5–10 flight legs available for the IHOP_2002 data. This necessitates an additional curve fitting step.

In contrast, the geostatistical method has the advantage of providing not only an estimate of the spatial variability, but also the non-spatial variability—often attributed as measurement error—and the total variability of the airborne observations. This method also provides an estimate of the practical range of spatial correlation among the measurement points. Furthermore, the geostatistical method provides information about the distribution of the data and the presence of nonstationary points; this, in turn, allows for analysis of the underlying causes of the variability. Given the advantages of the geostatistical method over the other techniques, the study suggests that it is the preferred statistical method to analyze the spatial variability of airborne-flux measurements.

The relationship between the slope of a plot of λE as a function of H and both A and the partition of the turbulent fluxes is confirmed. Moreover, because the data adhere to a characteristic slope, and, as discussed by LeMone et al. (2008), the deviations from that slope can be attributed to random error, the slope method can be used to both identify and correct values of H, λE, and hence G. In turn, this allows the source of variability in A to be identified. Our results demonstrate, for at least these five days with few or no clouds, that the variability in A and the partition of the fluxes is due primarily to variations in G, with R_n playing a secondary role. In turn, based on the supporting analysis with the surface data, G is controlled by T_{sfc}, vegetation density, and θ. Thus, in order to understand or model the spatial variability in the fluxes observed over the IHOP_2002 domain, an accurate description of these factors and their interactions is required.

The combination of the geostatistical method with the slope method has proven to be valuable to both quantifying and understanding the causes of the spatial variability in airborne-flux measurements over the IHOP_2002 domain. While additional analysis is needed to confirm their applicability, these tools may also be useful in understanding the variability in other environments. By better quantifying that variability, it should be possible to link the variability in the fluxes to the variability in surface characteristics. Ultimately, this may be useful to understanding the influence of surface variability on land-atmosphere exchange processes and subsequent meteorological, hydrological, and environment phenomena across a range of scales.

Acknowledgments The authors would like to thank M. O'Connell for her assistance during the course of this research. The authors would also like to thank the crew of the University of Wyoming King Air, the staff of NCAR-EOL and the University of Colorado without whom these data would not be available. The authors would like to acknowledge the support for IHOP_2002 and this research from USWRP, the NCAR Water Cycle Initiative (Grant NSF 01), NSF (ATM-0296159 and ATM-0236885), NASA GWEC (NNG05GB41G), NOAA JCSDA (NA06NES4400013), DOE ARM (08ER64674) and NASA Headquarters through the NASA Earth and Space Science Fellowship (NNX07AN67H). Alfieri would also like to acknowledge the support of the NCAR Advance Study Program and the NCAR Mesoscale and Microscale Meteorology Division Visiting Scientist Program.

References

Alfieri JG, Blanken PD, Yates DN, Steffen K (2007) Variability in the environmental factors driving evapotranspiration from a grazed rangeland during severe drought conditions. J Hydrometeorol 8:207–220

Anthes RA (1984) Enhancement of convective precipitation by mesoscale variations in vegetative covering in semiarid regions. J Clim Appl Meteorol 23:541–554

Chappell A, McTainsh G, Leys J, Strong C (2003) Using geostatistics to elucidate temporal change in the spatial variation of Aeolian sediment transport. Earth Surf Process Landf 28:567–585

Cressie N (1993) Statistics for spatial data. Wiley, New York, 928 pp

Diggle PJ, Ribeiro PJ, Christensen OF (2003) An introduction to model-based geostatistics. In: Møller J (ed) Spatial statistics and computational methods. Springer Verlag, New York, pp 43–86

Durre I, Wallace JM (2001) The warm season dip in diurnal temperature range over the Eastern States. J Clim 14:354–360

Ersahin S (2001) Assessment of spatial variability in nitrate leaching to reduce nitrate leaching to reduce nitrogen fertilizers impact on water quality. Agric Water Manage 48:179–189

Garrigues S, Allard D, Baret F, Weiss M (2006) Quantifying spatial heterogeneity at the landscape scale using variogram models. Remote Sens Environ 103:81–96

Goetz SJ (1997) Multisensor analysis of NDVI, surface temperature and biophysical variables at a mixed grassland site. Int J Remote Sens 18:71–94

Gutman G, Ignatov A (1997) Satellite derived green vegetation fraction for use in numerical weather predication models. Adv Space Res 19:477–480

Isaaks EH, Srivastava RM (1989) Applied geostatistics. Cambridge University Press, New York, 561 pp

Kint V, Van Meirvenne M, Nachtergale L, Geudends G, Lust N (2003) Spatial methods for quantifying forest stand structure development: a comparison between nearest-neighbor indices and variogram analysis. For Sci 49:36–49

LeMone MA, Grossman RL, Chen F, Ikeda K, Yates D (2003) Choosing the averaging interval for comparison of observed and modeled fluxes along aircraft transects of a heterogeneous surface. J Hydrometeorol 4:179–195

LeMone MA, Chen F, Alfieri JG, Tewari M, Geerts B, Miao Q, Grossman RL, Coulter RL (2007a) Influence of land cover and soil moisture on the horizontal distribution of sensible and latent heat fluxes in southeast Kansas during IHOP_2002 and CASES-97. J Hydrometeorol 8:68–87

LeMone MA, Chen F, Alfieri JG, Cuenca R, Niyogi D, Kang S, Davis K, Blanken PD (2007b) Surface, soil, and vegetation network during the international H2O project 2002 field campaign. Bull Am Meteorol Soc 88:65–81

LeMone MA, Tewari M, Chen F, Alfieri JG, Niyogi D (2008) Evaluation of the Noah land surface model using data from a fair-weather IHOP_2002 day with heterogeneous surface fluxes. Mon Weather Rev 136:4915–4941

Mahrt L, Vickers D, Sun J (2001) Spatial variations of surface moisture flux from aircraft data. Adv Water Resour 24:1133–1141

Mann J, Lenschow DH (1994) Errors in airborne flux measurements. J Geophys Res 99:14519–14526

Matern B (1986) Spatial variation, lecture notes in statistics, vol 36. Springer-Verlag, New York, 151 pp

McPherson RA (2007) A review of vegetation-atmosphere interactions and their influence on mesoscale phenomena. Prog Phys Geogr 31:261–285

Oncley SP, Lenschow DH, Campos TL, Davis KJ, Mann J (1997) Regional-scale surface flux observations across the boreal forest during BOREAS. J Geophys Res 102:29147–29154

Peters-Lidard CD, Blackburn E, Liang X, Wood EF (1998) The effect of soil thermal conductivity parameterization on surface energy fluxes and temperatures. J Atmos Sci 55:1209–1224

Pielke RA (2001) Influence of the spatial distribution of vegetation and soils on the prediction of cumulus convective rainfall. Rev Geophys 39:151–177

Pielke RA, Adegoke J, Beltran-Przekurat A, Hiemstra CA, Lin J, Nair US, Niyogi D, Nobis TE (2007) An overview of regional land use and land cover impacts on rainfall. Tellus B 59:587–610

Raddatz RL (2005) Moisture recycling on the Canadian prairies for summer droughts and pluvials from 1997–2003. Agric Meteorol 131:13–26

Raddatz RL (2007) Evidence for the influence of agriculture on weather and climate through the transformation and management of vegetation: illustrated by examples from the Canadian Prairies. Agric Meteorol 142:186–202

Sandholt I, Rasmussen K, Andersen J (2002) A simple interpretation of the surface temperature/vegetation index space for assessment of surface moisture status. Remote Sens Environ 79:213–224

Santanello JA, Friedl MA, Ek MB (2007) Convective planetary boundary layer interactions with the land surface at diurnal time scales: diagnostics and feedbacks. J Hydrometeorol 8:1082–1097

Schabenberger O, Gotway CA (2005) Statistical methods for spatial data analysis. Chapman & Hall, Boca Raton, 516 pp
Segal M, Avissar R, McCumber MC, Pielke RA (1988) Evaluation of vegetation effects on the generation and modification of mesoscale circulations. J Atmos Sci 45:2268–2292
Sellers PJ, Heiser MD, Hall FG, Goetz SJ, Strebel DE, Verma SB, Desjardins RL, Schuepp PM, MacPherson JI (1995) Effects of spatial variability in topography, vegetation cover and soil moisture on area-averaged surface fluxes: a case study using the FIFE 1989 data. J Geophys Res 100:25607–25629
Sertel E, Kaya S, Curran PJ (2007) Use of semivariograms to identify earthquake damage in an urban area. Trans Geosci Remote Sens 45:1590–1594
Small EE, Kurc SA (2003) Tight coupling between soil moisture and the surface radiation budget in semiarid environments: implications for land-atmosphere interactions. Water Resour Res 39:1278–1291
Song J, Wesley M (2003) On comparison of modeled surface flux variations to aircraft observations. Agric Meteorol 117:159–171
Stassberg D, LeMone MA, Warner T, Alfieri JG (2008) Comparison of observed 10 m wind speeds to those based on Monin-Obukhov similarity theory using aircraft and surface data from the International H2O Project. Mon Weather Rev 136:964–972
Tarnavsky E, Garrigues S, Brown ME (2008) Multiscale geostatistical analysis of AVHRR, SPOT-VGT, and MODIS global NDVI products. Remote Sens Environ 112:535–549
Webb EK, Pearlman GI, Leuning R (1980) Correction of flux measurements for density effects due to heat and water vapor transfer. Q J Roy Meteorol Soc 106:85–100
Weckworth TM, Parsons DB, Koch SE, Moore JA, LeMone MA, Demoz BB, Flamant C, Geerts B, Wang J, Feltz WF (2004) An overview of the international H2O project (IHOP_2002) and some preliminary highlights. Bull Am Meteorol Soc 85:253–277
Wilczak J, Oncley S, Stage SA (2001) Sonic anememoeter tilt correction algorithms. Boundary-Layer Meteorol 99:127–150
Woodcock CE, Strahler AH, Jupp LB (1988a) The use of variograms in remote sensing: scene models and simulated images. Remote Sens Environ 25:323–348
Woodcock CE, Strahler AH, Jupp LB (1988b) The use of variograms in remote sensing: real digital images. Remote Sens Environ 25:349–379
Zhang H (2004) Inconsistent estimation and asymptotically equal interpolation in model-based geostatistics. J Am Stat Assoc 99:250–261
Zhang H, Zimmerman D (2007) Hybrid estimation of semivariogram parameters. Math Geol 39:247–260
Zimmerman DL, Zimmerman MB (1991) A comparison of spatial semivariogram estimators and corresponding ordinary kriging predictors. Technometrics 33:77–91